Brief Report

Thermoelectric Field Analysis of Trapezoidal Thermoelectric Generator Based on the Explicit Analytical Solution of Annular Thermoelectric Generator

Wei Niu and Xiaoshan Cao *

School of Civil Engineering and Architecture, Xi'an University of Technology, Xi'an 710048, China; niuwei1141542660@163.com
* Correspondence: caoxsh@xaut.edu.cn

Abstract: The geometrical configuration is one of the main factors that affect the thermoelectric performance of a device. Research on the trapezoidal thermoelectric generator (TTEG) with varied cross section is mainly based on finite element simulation and experiment. In this paper, an explicit analytical solution of the maximum output power of annular thermoelectric generators (ATEG) is proposed, which has been proved to have high accuracy. Then, the maximum output power between ATEG and TTEG is compared. Results show that, for the appropriate geometric parameter δ, the relative error of maximum output power between explicit analytical ATEG and the simulated solution of TTEG can reach the order of 10^{-3}. When the hot end is at the a side, the high temperature and θ is 510 K and 10°, respectively. For Bi_2Te_3 material and PbTe material, the relative error of maximum output power between the explicit analytical and simulated solution is 0.0261% and 0.074%, respectively. Under suitable working conditions, the explicit analytical results of ATEG can provide some reference for the performance optimization of TTEG.

Keywords: trapezoidal thermoelectric generator; annular thermoelectric generator; varied cross section; explicit analytical solution; output power

1. Introduction

In the early nineteenth century, scientists discovered the thermoelectric effect, which enables the direct conversion of heat and electricity. With the increasing demand for applications, such as industrial waste energy and recovery (genetic algorithm optimization [1], experimental investigation [2], comparative study [3]), automobile exhaust recovery and treatment (numerical analysis [4], economic optimization [5], experimental investigation [6]), self-supplied energy in space stations (aircraft power system [7], radioisotope power system [8]), self-generation of flexible wearable devices [9], solar photovoltaic system [10], and other aspects of architecture engineering (integrated energy systems [11], multi-energy building microgrid [12]), on the basis of the thermoelectric effect, thermoelectric generators (TEGs) that realize heat and electric energy conversion with a certain temperature difference structure have received wide attention from researchers. TEGs can not only achieve direct conversion of energy, but also have the advantages of environmental protection, no pollution, no noise, no moving parts, good stability, and are maintenance free. Based on the above reasons, the application of TEGs can effectively alleviate today's energy shortage problems. An important index to evaluate the performance of a TEG is the dimensionless thermoelectric figure of merit (*ZT*) of the thermoelectric material (TEM). Many thermoelectric materials are also being explored for power generation applications, such as GeTe [13,14], PbTe [15], and silicides [16]. To improve the *ZT* value of TEM, researchers have proposed different optimization methods. At the thermoelectric materials' level, Mahan [17] introduced a numerical simulation method to investigate the temperature field distribution and the *ZT* value in TEGs with functionally graded materials (FGM), and the theoretical calculations

results showed that, inhomogeneous doping can improve the energy efficiency of TEGs. Kuznetsov [18] investigated the power generation of high-performance FGMs and segmented materials by using double doping technology, and the results showed that using FGMs and layered materials can effectively improve the energy conversion of thermoelectric generators for low-temperature waste heat recovery. Wallace [19] investigated the efficiency of a sandwiched TEM and found that the efficiency is influenced by the location and gradation profile of the graded interlayer. Jin [20] studied the energy efficiency of TEGs with exponentially graded thermoelectric material, and obtained the closed-form solution of the temperature field distribution of functionally graded TEGs; the results showed that the conversion efficiency may be increased by about 30% by using appropriate property gradients. Cao proposed a power series method and power series iterative approximation method to obtain the temperature field distribution of FGM TEGs with temperature-independent and temperature-dependent materials, and both the power series solution [21] and the power series iterative approximate solution [22] have been verified to have high accuracy and stability. On the basis of the research results on flat TEGs, this research group then studied the temperature field distribution of an annular thermoelectric generator (ATEG) composed of FGMs (temperature independent [23] and temperature dependent [24]). In addition to TEMs, from the device level, the geometry and cross-sectional design of thermoelectric legs are important for the improvement of the thermoelectric performance. By using ANSYS software, when the varying inlet temperature, velocity and the connective heat transfer coefficient are considered, Zhang [25] compared annular and flat-plate TEGs (FTEG) for cylindrical hot source, and found that the ATEG has obvious advantages over the FTEG. Dizaji [26] proposed a thin-film flexible solar TEG to identify the effects of all parameters on thermoelectric performance by using a 3D numerical simulation. The simulated results showed that the intensity of the output power first increases and then decreases with the increase in the number of legs, and for output power, the impact of leg thickness was more effective than the impact of leg length. Fateh [27] proposed a finite difference model to study the interdependencies between optimization parameters such as TE element leg length, fill fraction, leg area ratio between n- and p- type legs, and load resistance. The results showed that a smaller number of shorter legs has a higher potential than a greater number of longer legs to achieve the same power per unit module area. Shi [28] analyzed the nominal power density of thermoelectric pins with non-constant cross sections and found that pins with linear variation in the cross section have higher nominal power density than those with quadratic and exponential cross-sectional legs. Ali [29] analyzed the influence of pin leg geometry on energy conversion efficiency and output power of the thermoelectric device and found that increasing the dimensionless geometric parameter improves the efficiency of the device under the different temperature ratios and external load resistance ratios. To prove that the geometrical configuration of thermoelectric legs can improve the thermoelectric performance of the devices, Fabian-Mijangos [30] designed a proof-of-concept experiment to confirm that the figure of merit of a thermoelectric device with asymmetrical legs is almost twofold that of a traditional one with a constant square cross section. Niu [31] introduced asymmetric configuration to the transport junction, and they found that the figure of merit of optimized asymmetric thermoelectric devices is five times than that of the *ZT* value of symmetric configuration. The results demonstrated that the asymmetry of the transport junction can enhance the thermoelectric efficiency effectively. In summary, to accomplish the geometric optimization of the device, the geometry of the legs [32], leg length [33], and number of legs [34] are taken into account. In sum, most researchers use the explicit analytical method to solve temperature-independent TEGs to address the temperature field and energy conversion of TEGs with symmetric cross-sectional legs. Moreover, most researchers use the finite element simulation method when considering the temperature dependence of materials.

A thermoelectric device composed of trapezoidal thermoelectric legs (legs with non-constant cross sections) cannot obtain an explicit analytical solution. When the dependence of the temperature of thermoelectric materials is considered, the thermoelectric coupled

field is nonlinear. For the analysis of nonlinear coupled fields, the existing research mostly uses numerical methods to solve the field governing equation, and the analytical solutions have irreplaceable advantages. Especially for muti-parameter coupling problems, the explicit analytical solution is convenient to clarify the influence of each parameter on the field quantity to be solved in the structure. Thus, in this work, we propose an idea that enables the explicit analytical solution of the ATEG to approximate the solution of the TTEG under suitable operating conditions, which can provide some guidance for improving the performance of variable cross-section thermoelectric devices.

2. Basic Thermoelectric Models

The basic model of TEGs with an external resistance (R_L) is shown in Figures 1 and 2. Figures 1 and 2a show a schematic illustration of an annular TEG (ATEG) and trapezoid TEG (TTEG), respectively. Depending on the shape of the thermoelectric legs of the TEGs, the two TEGs are composed of p-type and n-type legs that are identical, except that they are oppositely doped. We focus on the lower leg, which is composed of temperature-dependent TEM. To simplify the calculation, we assume that the annular thermoelectric model is an approximate axisymmetric model. In Figure 1, a and b are the inner and outer diameter of the ring, respectively.
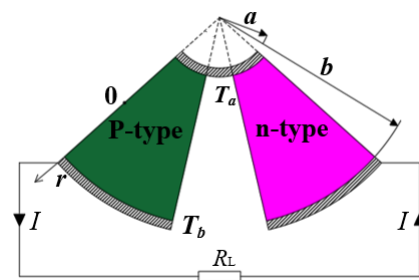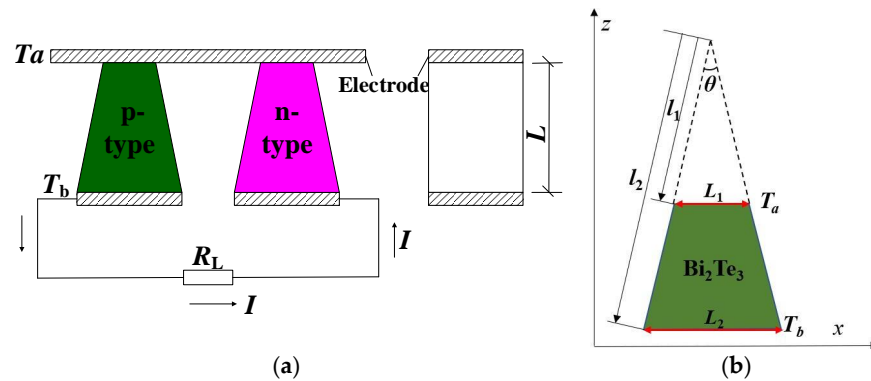

Figure 1. Basic model of ATEG.

(**a**)   (**b**)

Figure 2. Schematic of (**a**) trapezoidal thermoelectric generator and (**b**) thermoelectric legs.

2.1. Mathematical Models of ATEG

In 2D cylindrical coordinate system, the basic equations are as follows:

$$\boldsymbol{J} = -\frac{\nabla \varphi}{\rho} - \frac{S}{\rho} \nabla T \tag{1}$$

$$\boldsymbol{q} = S T \boldsymbol{J} - k \nabla T \tag{2}$$

$$\nabla \cdot \boldsymbol{q} = \boldsymbol{J} \cdot \boldsymbol{E} \tag{3}$$

$$\nabla \cdot \boldsymbol{J} = 0 \tag{4}$$

where $\boldsymbol{J}$, $\boldsymbol{q}$, and $\boldsymbol{E}$ are the current density vector, heat flux vector, and electric field vector, respectively. S, k, ρ are the Seebeck coefficient, thermal conductivity, and electrical resistivity, respectively. φ is the electric potential. T is the absolute temperature.

On the basis of Equation (4), it can be rewritten as

$$\frac{\mathrm{d}(rJ_r)}{r\mathrm{d}r} = 0 \tag{5}$$

where J_r is the current density along the r direction. Hereafter, subscript r represents the component of the variable along the r direction.

The solution to Equation (5) is

$$J_r = \frac{H_0}{r} \tag{6}$$

where H_0 is the relative current density, which is an uncertain constant, and the unit is A/m.

With Equations (1) and (2) substituted into Equation (3), the governing equation of the temperature field is

$$kr^2\frac{\mathrm{d}^2T}{\mathrm{d}r^2} + r^2\frac{\mathrm{d}k}{\mathrm{d}r}\frac{\mathrm{d}T}{\mathrm{d}r} - H_0r\frac{\mathrm{d}S}{\mathrm{d}r}T + kr\frac{\mathrm{d}T}{\mathrm{d}r} + \rho H_0{}^2 = 0 \tag{7}$$

The boundary conditions of the temperature field are

$$T(a) = T_a, T(b) = T_b \tag{8}$$

when the cold end is located at side a, that is, $T_a = T_\mathrm{C}$, $T_b = T_\mathrm{H}$. (T_C and T_H represent the cold and high temperature, respectively).

When the initial temperature field is given as follows:

$$T^* = \frac{T_\mathrm{C} + T_\mathrm{H}}{2} + \frac{(T_\mathrm{H} - T_\mathrm{C})\bar{r}}{\delta} \tag{9}$$

where

$$\bar{r} = \frac{r}{a} - 1 - \frac{b-a}{2a}, \delta = \frac{b}{a} - 1, \bar{r} \in \left[-\frac{\delta}{2}, \frac{\delta}{2}\right] \tag{10}$$

Based on Equations (9) and (10), Equation (7) can be written as

$$r^2\frac{\mathrm{d}}{\mathrm{d}r}\left(k\frac{\mathrm{d}T}{\mathrm{d}r}\right) + rk\frac{\mathrm{d}T}{\mathrm{d}r} + \left(\rho^* H_0{}^2 - H_0 r\frac{\mathrm{d}S^*}{\mathrm{d}r}T^*\right) = 0 \tag{11}$$

where S^*, ρ^* are the Seebeck coefficient and electrical resistivity under the initial temperature field, respectively.

Let

$$y = r\left(k\frac{\mathrm{d}T}{\mathrm{d}r}\right), g(r) = \rho^* H_0{}^2 - H_0 r\frac{\mathrm{d}S^*}{\mathrm{d}r}T^* \tag{12}$$

Equation (11) can be written as

$$r\frac{\mathrm{d}y}{\mathrm{d}r} + g(r) = 0 \tag{13}$$

By solving Equation (13), we can obtain

$$y(r) = -\int_{r_1}^{r}\frac{g(r)}{r}\mathrm{d}r + C_1 \tag{14}$$

where C_1 is an uncertain constant, which can be determined by boundary conditions.

When Equations (2) and (6) are combined, the component of heat flux along the r direction is

$$q_r = -k\frac{dT}{dr} + ST\frac{H_0}{r} \tag{15}$$

When side a is the cold side, let

$$Y = bq(b) - aq(a) \tag{16}$$

By solving Equation (16), we can obtain the following:

$$
\begin{aligned}
Y &= y(a) - y(b) + (STH_0|_{r=b} - STH_0|_{r=a}) \\
&= \int_a^b \frac{\rho^* H_0{}^2}{r}dr - \int_a^b H_0\frac{dS^*}{dr}T^*dr + (ST|_{r=b} - ST|_{r=a})H_0
\end{aligned} \tag{17}
$$

Let

$$\frac{dY}{dH_0} = 0 \tag{18}$$

By solving Equation (18), we can obtain $\widetilde{Y}$ and $\widetilde{H}_0$ as follows:

$$\widetilde{H}_0 = \frac{\int_a^b \frac{dS^*}{dr}T^*dr + ST|_{r=a} - ST|_{r=b}}{\int_a^b \frac{2\rho^*}{r}dr} = \frac{-\frac{(T_b - T_a)}{b-a}\int_a^b S^*dr}{\int_a^b \frac{2\rho^*}{r}dr} \tag{19}$$

$$\widetilde{Y} == \int_a^b \frac{\rho^* \widetilde{H}_0{}^2}{r}dr - \int_a^b \widetilde{H}_0\frac{dS^*}{dr}T^*dr + (ST|_{r=b} - ST|_{r=a})\widetilde{H}_0 \tag{20}$$

The thickness of the module selected in this analysis is the unit thickness; thus, the maximum output power can be expressed as follows:

$$P_{\text{out max}} = 4\pi\widetilde{Y} \times 10^{-3} \tag{21}$$

When side a is the hot side, we can obtain

$$\widetilde{H}_0 = \frac{\int_b^a \frac{dS^*}{dr}T^*dr + ST|_{r=b} - ST|_{r=a}}{\int_b^a \frac{2\rho^*}{r}dr} = \frac{-\frac{(T_b - T_a)}{a-b}\int_b^a S^*dr}{\int_b^a \frac{2\rho^*}{r}dr} \tag{22}$$

$$\widetilde{Y} = \int_b^a \frac{\rho^* \widetilde{H}_0{}^2}{r}dr - \int_b^a \widetilde{H}_0\frac{dS^*}{dr}T^*dr + (ST|_{r=a} - ST|_{r=b})\widetilde{H}_0 \tag{23}$$

2.2. Numerical Models of TTEG

The numerically analyzed thermoelectric modules in this work have trapezoid legs composed of Bi$_2$Te$_3$ materials, as shown in Figure 2. To obtain the absorbed heat energy Q_{in} at the hot end and the output power of the TTEG, the finite element method based on a COMSOL thermoelectric module is applied to solve the governing equations that describe temperature and potential distribution and thermoelectric coupling effects, as shown in Equations (24) and (25). After the calculation of the software, the output power $\widetilde{P}_{\text{out}}$ and conversion efficiency η are obtained by

$$\nabla(k\nabla T) - T\vec{J}\left[\left(\frac{\partial S}{\partial T}\right)\nabla T + (\nabla S)_T\right] = -\rho\vec{J}^2 \tag{24}$$

$$\nabla\left(\frac{\nabla E}{\rho} + \frac{S\nabla T}{\rho}\right) = 0 \tag{25}$$

$$\widetilde{P}_{\text{out}} = I^2 R_L \frac{360^\circ}{\theta} = \frac{S^2(T_H - T_C)^2 R_L}{(R_L + R)^2}\frac{360^\circ}{\theta}, \eta = \frac{\widetilde{P}_{\text{out}}}{Q_{in}} \tag{26}$$

where R is the resistance of the thermoelectric generator.

3. Results and Discussion

The explicit analytical solution of the governing equations of the TTEG cannot be obtained. Thus, we aim to optimize and design the performance of the TTEG based on the explicit analytical solution of the ATEG.

Let

$$b = a(1 + \delta), L_1 = l_1 \frac{\theta}{180°} \pi, L_2 = l_2 \frac{\theta}{180°} \pi \tag{27}$$

where a and b are the inner and outer diameter of the ring, respectively. δ is a small quantity, $a = l_1 = 5$ mm, and $b = l_2$.

3.1. Verification of the Explicit Analytical Solution of ATEG

For verification, we compare the explicit analytical solution and the power series iteration approximate (PSIA) solution in Ref. [20], which has been proven to have high accuracy. One kind of TE material, namely, regular Bi_2Te_3, is introduced. Thermal conductivity k, the Seebeck coefficient S, and electrical resistivity ρ satisfy the following:

$$
\begin{aligned}
k &= k_0 \left[1 + \alpha_1{}^k \left(\frac{T-T_0}{T_0} \right) + \alpha_2{}^k \left(\frac{T-T_0}{T_0} \right)^2 + \alpha_3{}^k \left(\frac{T-T_0}{T_0} \right)^3 \right] \\
S &= S_0 \left[1 + \alpha_1{}^S \left(\frac{T-T_0}{T_0} \right) + \alpha_2{}^S \left(\frac{T-T_0}{T_0} \right)^2 + \alpha_3{}^S \left(\frac{T-T_0}{T_0} \right)^3 \right] \\
\rho &= \rho_0 \left[1 + \alpha_1{}^\rho \left(\frac{T-T_0}{T_0} \right) + \alpha_2{}^\rho \left(\frac{T-T_0}{T_0} \right)^2 + \alpha_3{}^\rho \left(\frac{T-T_0}{T_0} \right)^3 \right]
\end{aligned}
\tag{28}
$$

where $T_0 = 300$ K. For regular Bi_2Te_3,
$k_0 = 0.9658$ W/mK, $\alpha_1{}^k = 0.4452$, $\alpha_2{}^k = -2.2547$, $\alpha_3{}^k = 2.9601$,
$S_0 = 174.1$ μV/K, $\alpha_1{}^S = 0.9386$, $\alpha_2{}^S = -1.3375$, $\alpha_3{}^S = 0.2693$,
$\rho_0 = 0.934 \times 10^{-5}$ Ωm, $\alpha_1{}^\rho = 1.0494$, $\alpha_2{}^\rho = 5.5779$, $\alpha_3{}^\rho = -5.8316$.

Figure 3a shows that the output power of the explicit analytical solution and PSIA solution under different current densities. From the figure, it can be seen that the explicit analytical solution of the annular TEG is highly consistent with the PSIA solution. The calculation indicates that the relative error of $\widetilde{Y}$ first increases and then decreases with the increase in the high temperature. The maximum E_R of $\widetilde{Y}$ between analytical solution and PSIA solution is 0.93%, as shown in Figure 3b.
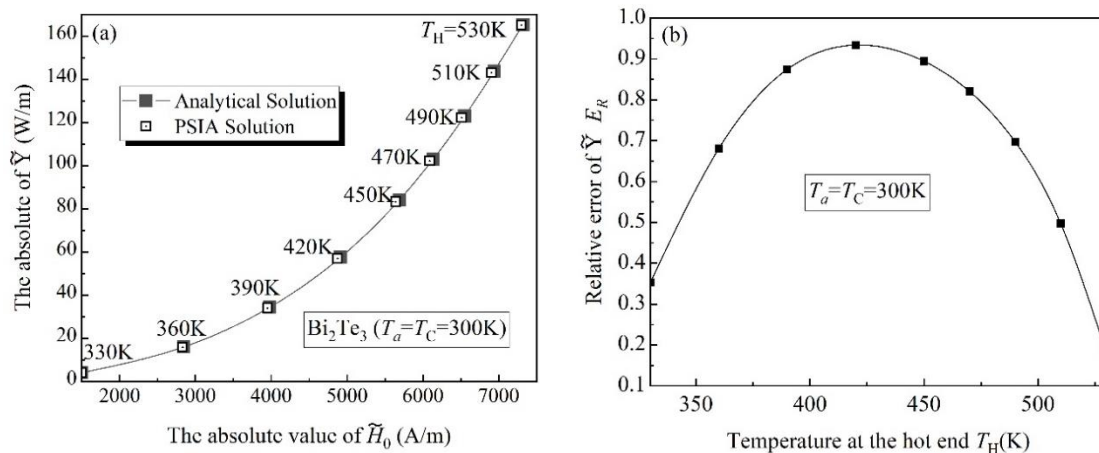

Figure 3. Comparison between explicit analytical and PSIA solution, (**a**) $\widetilde{Y}$ versus $\widetilde{H}_0$; (**b**) E_R of $\widetilde{Y}$ at different hot temperatures.

3.2. Thermoelectric Performance of TTEG

#### 3.2.1. Numerical Simulation Results of TTEG

In this section, the performance of the TTEG is studied through finite element simulation on 3D geometries by using COMSOL software, when the high temperature is 530 K, and the low temperature is 300 K. As shown in Figure 4, when the load resistance remains constant, as the θ value increases, the current, terminal voltage, and output power also increase. It can be seen that, in Figure 4a, the current in the circuit monotonically decreases as the load resistance increases. When the load resistance researches 0.4 Ω, the current values reach the same level (0.21 A), at different θ values. From Figure 4b, contrary to the trend of current variation, we can see that the terminal voltage monotonically increases as the load resistance increases. When the load resistance reaches 1 Ω, the terminal voltage in the circuit of thermoelectric devices at different θ values can reach 0.087 V. Unlike the monotonic variation trend of current and voltage, as shown in Figure 4c, the output power of thermoelectric generator first increases and then decreases as the load resistance increases. This phenomenon can also be explained from Equation (26), where when the load resistance (R_L) matches the resistance of the generator itself (R), that is $R_L/R = 1$, the load can obtain the maximum output power from the generator. When the output power reaches a peak at various values of θ, the load resistance is between 0.02 Ω and 0.04 Ω.
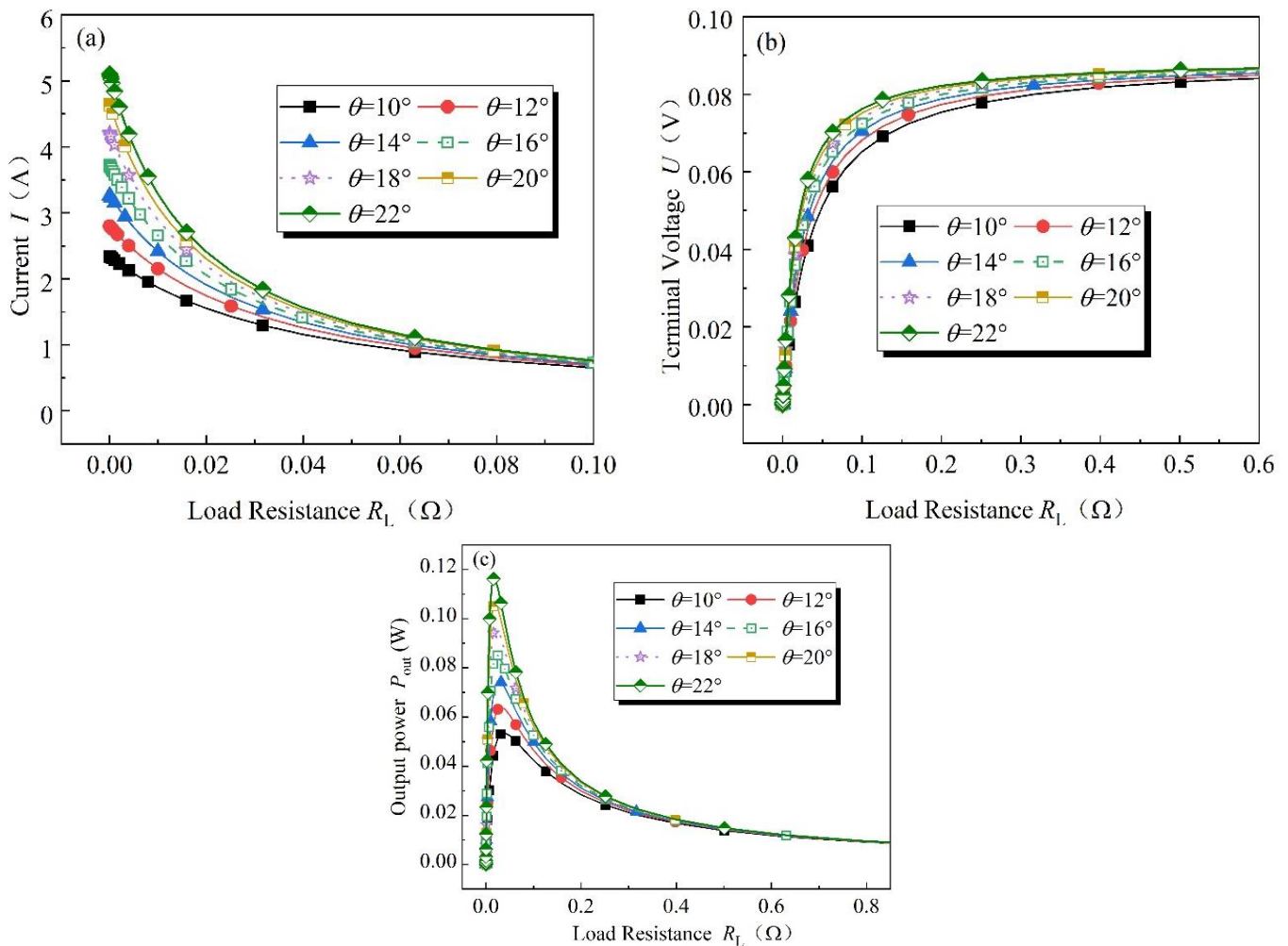
Figure 4. (**a**) The relationship between current and resistance load; (**b**) terminal voltage and resistance load; and (**c**) output power and resistance load.

3.2.2. Comparison of Thermoelectric Performance between TTEG and ATEG

A module with a pair of annular legs is introduced and used as the reference module to compare the thermoelectric performance. Figure 5 shows the temperature distribution of the TTEG, indicating that the temperature shows an approximate linear change trend with the coordinate position, which is similar to the trend of temperature field distribution of the ATEG in Ref. [24] (where the dimensionless position $\bar{z}$ is the ratio of the coordinate value of a certain point of the thermoelectric leg to the total length during the modeling process).
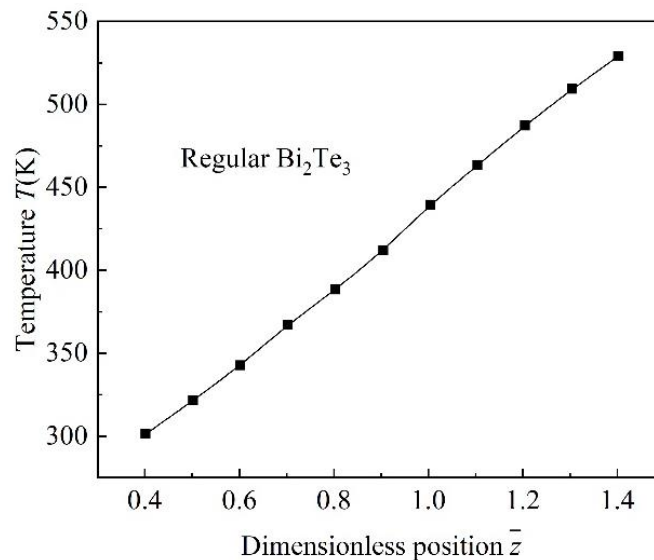
Figure 5. Temperature distribution of TTEG.

To make the explicit analytical solution of the ATEG more approximate to the simulated solution of the TTEG, we seek the best value of δ to minimize the relative error between the explicit analytical solution and the simulated solution, and verify that the explicit analytical solution of the ATEG can replace the simulated solution of the TTEG approximately, thus providing a reference for the optimization and design of the TTEG.

E_R is defined as follows:

$$E_R = \frac{\left| P_{out} - \widetilde{P}_{out} \right|}{\widetilde{P}_{out}} \tag{29}$$

where P_{out} is the explicit analytical solution of output power of the ATEG, $\widetilde{P}_{out}$ is the simulated solution of output power of the TTEG, and E_R is the relative error between the ATEG and TTEG.

For Bi_2Te_3 material, when the high temperature is 530 K and the low temperature is 300 K, Table 1 gives the explicit analytical solution of the ATEG and simulated solution of the TTEG under different δ to achieve the $P_{out\,max}$. Figure 6 shows the relationship between the explicit analytical solution of the ATEG and simulated solution of the TTEG at different angles of θ when the value of δ reaches the optimal value. According to Table 1 and Figure 6, under different geometric dimensions, the explicit analytical solution of the ATEG is in good agreement with the simulated solution of the TTEG when the coefficient of δ reaches the optimal value. When $T_C = 300$ K, $\theta = 10$, the high temperature varies from 450 K to 530 K, the variation curve of $P_{out\,max}$ and voltage with current is shown in Figure 7 (I and V in the figure represent the corresponding current and voltage at $P_{out\,max}$, respectively). In Figure 7, we can know that when $T_H = 490$ K, the relative error of $P_{out\,max}$, I and V are 0.226%, 0.80% and 0.58%, respectively. As shown in Figure 8, for $T_a = T_H$, the maximum relative error between the explicit analytical solution and simulated solution is 0.18%; for $T_a = T_C$, the maximum relative error is 0.17%. For $T_a = T_H$, when $12° \leq \theta \leq 18°$, the relative error

between them reaches the order of 10^{-3}. For $T_a = T_C$, when $\theta \in \left[12^{\circ}, 14^{\circ}\right], \left[20^{\circ}, 22^{\circ}\right]$, the relative error can also reach the order of 10^{-3}.

**Table 1.** Optimal value of δ under different angles of θ. ($T_a = T_H / T_a = T_C$).

θ (°)	δ	$P_{\text{out max}}$ (W)	$\widetilde{P}_{\text{out max}}$ (W)
10	0.211/0.218	1.921849/1.923000	1.925166/1.925009
12	0.211/0.218	1.921849/1.923000	1.921849/1.921200
14	0.212/0.219	1.913479/1.915156	1.914718/1.914305
16	0.212/0.219	1.913479/1.915156	1.912410/1.911969
18	0.211/0.218	1.921849/1.923000	1.920569/1.920007
20	0.213/0.220	1.905187/1.907383	1.907013/1.906528
22	0.213/0.221	1.905187/1.899680	1.901673/1.901009
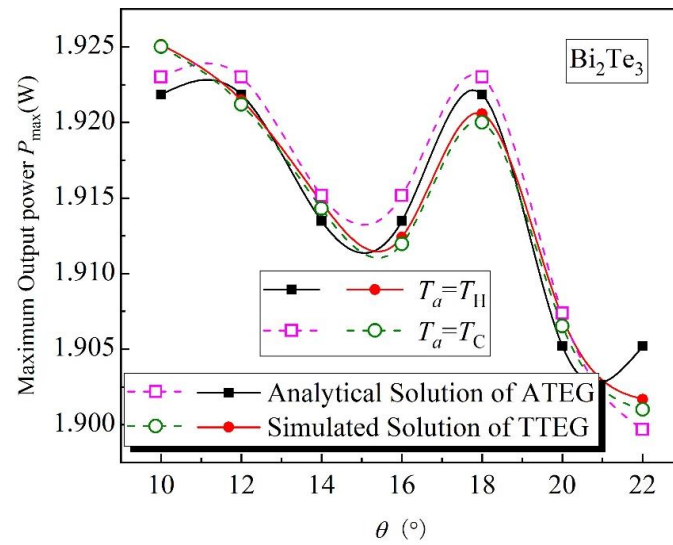
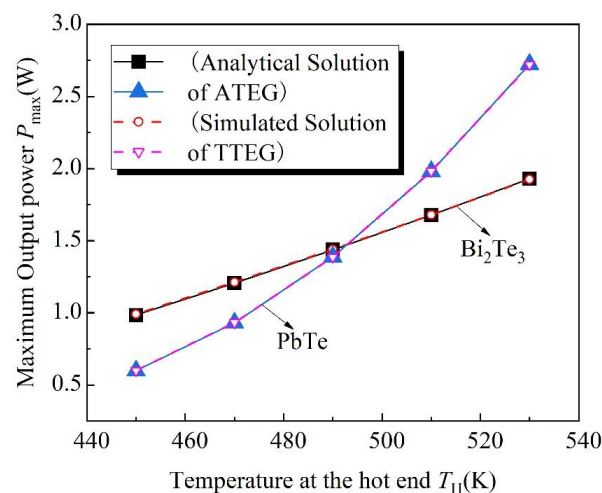**Figure 6.** Maximum output power under different values of θ.
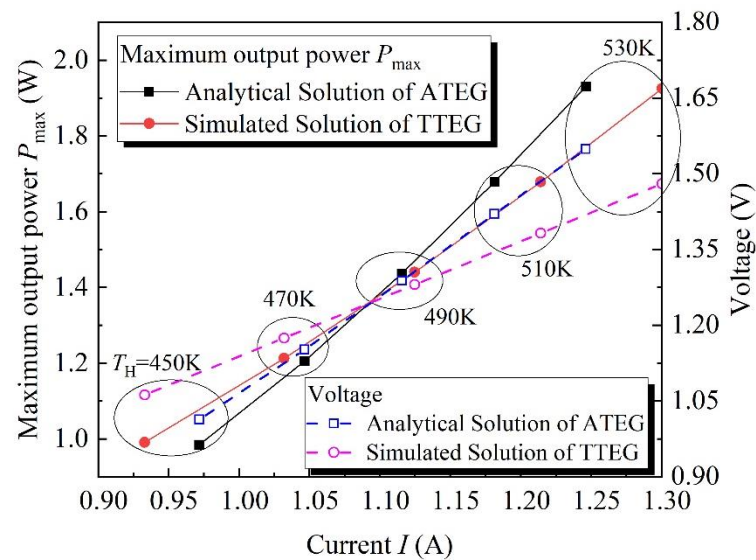
Figure 7. *P-I* and *V-I* curves under different temperature gradients when T_C = 300 K.
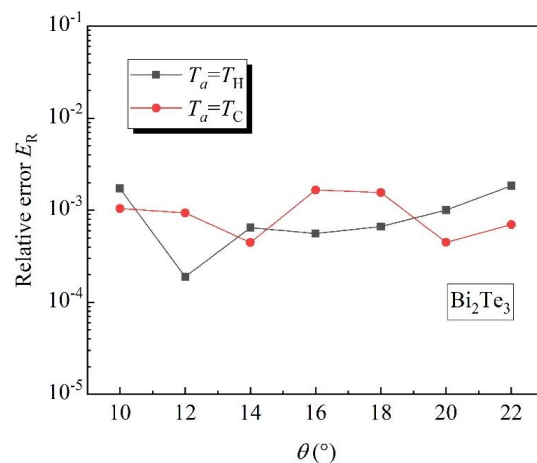
Figure 8. Relative error of explicit analytical and simulated solution after different angles of θ.

Finally, for a low temperature equal to 300 K and a high temperature at the *a* sides (450 K–530 K), when $\theta = 10°$, we calculate the maximum output power versus high temperature with different thermoelectric materials, as shown in Figure 9. As the temperature at the hot end increases, the output power peak increases. When the δ reaches the optimal value, the explicit analytical solution is highly consistent with the simulated solution regardless of Bi_2Te_3 material or PbTe material. When the temperature at the hot end is 450 K, 470 K, 490 K, 510 K, and 530 K, for the maximum output power of Bi_2Te_3 material, the explicit analytical solution of the ATEG is 1.9218, 1.6782, 1.4432, 1.2108, and 0.9890 W, and the simulated solution of TTEG is 1.9252, 1.6786, 1.4401, 1.2126, and 0.9910 W. For the maximum output of PbTe material, the explicit analytical solution of the ATEG is 2.7235, 1.9799, 1.3884, 0.9302, and 0.5990 W, and the simulated solution of the TTEG is 2.7206, 1.9814, 1.3870, 0.9316, and 0.5991 W. A low temperature at the hot end can lead to a low maximum output power.

Based on the above content, we can know that the explicit analytical solution of the ATEG can clarify the influence of various material parameters on the performance of the device and avoid traversal calculations, but the solving process is relatively complex. The simulated solution of the TTEG avoids the complexity of solving a nonlinear differential equation, but it cannot intuitively clarify the impact of various material parameters on performance of the device. By solving the relative errors of $P_{\text{out max}}$, I and V between the ATEG and TTEG, it can be seen that under appropriate temperature gradients and geometric dimensions, the analytical solution of the ATEG can provide some guidance for further optimization design of the TTEG.

Figure 9. Maximum output power versus high temperature of different TEM.

4. Conclusions

In this work, an explicit analytical method for an ATEG that has symmetrical legs and a numerical simulation method for a TTEG that has varied cross sections was proposed to study the thermoelectric performance of thermoelectric devices. The explicit analytical solution has a high accuracy when the ATEG is composed of homogeneous materials. A comparison between the explicit analytical solution of the ATEG with the numerical solution of the TTEG shows that when the hot temperature is at the *a* side and is varied from 450 K to 530 K, for the relative error between the explicit analytical solution of the ATEG and the simulated solution of the TTEG, the maximum relative error of Bi_2Te_3 and PbTe is 0.21% and 0.15%, respectively. Thus, the results prove that the explicit analytical solution of the ATEG could provide guidance for the solution of the TTEG, thus opening a new route to the development and optimization of the TTEG.

Nomenclature

R_L	load resistance, (Ω)
J_r	electric current density along *r* direction, (Am^{-2})
H_0	relative electric current density, (Am^{-1})
E	electric field, (Vm^{-1})
k	thermal conductivity, ($Wm^{-1} K^{-1}$)
S	Seebeck coefficient, (VK^{-1})
ρ	electrical resistivity, (Ωm)
T	absolute temperature, (K)
P_{out}	analytical solution of output power of ATEG
$\widetilde{P}_{out}$	simulated solution of output power of TTEG
Subscript	
C	cold end of the TE leg
H	hot end of the TE leg
r	variables along the *r* direction

References

1. Bélanger, S.; Gosselin, L. Multi-objective genetic algorithm optimization of thermoelectric heat exchanger for waste heat recovery. *Int. J. Energy Res.* **2012**, *36*, 632–642. [CrossRef]
2. Tang, S.; Wang, C.; Liu, X.; Su, G.; Tian, W.; Qiu, S.; Zhang, Q.; Liu, R.; Bai, S. Experimental investigation of a novel pipe thermoelectric generator for waste heat recovery and electricity generation. *Int. J. Energy Res.* **2020**, *44*, 7450–7463. [CrossRef]
3. Yazawa, K.; Shakouri, A.; Hendricks, T.J. Thermoelectric heat recovery from glass melt processes. *Energy* **2017**, *118*, 1035–1043. [CrossRef]
4. Niu, Z.; Diao, H.; Yu, S.; Jiao, K.; Du, Q.; Shu, G. Investigation and design optimization of exhaust-based thermoelectric generator system for internal combustion engine. *Energy Convers. Manag.* **2014**, *85*, 85–101. [CrossRef]
5. Zhu, W.C.; Yang, W.L.; Yang, Y.; Li, Y.; Li, H.; Yan, Y.G.; Xie, C.J. Economic configuration optimization of onboard annual thermoelectric generators under multiple operating conditions. *Renew. Energy* **2022**, *197*, 486–499. [CrossRef]
6. Lu, H.; Wu, T.; Bai, S.; Xu, K.; Huang, Y.; Gao, W.; Yin, X.; Chen, L. Experiment on thermal uniformity and pressure drop of exhaust heat exchanger for automotive thermoelectric generator. *Energy* **2013**, *54*, 372–377. [CrossRef]

7.   Samson, D.; Kluge, M.; Becker, T.; Schmid, U. Wireless sensor node powered by aircraft specific thermoelectric energy harvesting. *Sens. Actuators A Phys.* **2011**, *172*, 240–244. [CrossRef]
8.   Lange, R.G.; Carroll, W.P. Review of recent advances of radioisotope power systems. *Energy Convers. Manag.* **2008**, *49*, 393–401. [CrossRef]
9.   Elmoughni, H.M.; Menon, A.K.; Wolfe, R.M.W.; Yee, S.K. A textile-integrated polymer thermoelectric generator for body heat harvesting. *Adv. Mater. Technol.* **2019**, *4*, 1800708. [CrossRef]
10. Yin, E.; Li, Q. Achieving extensive lossless coupling of photovoltaic and thermoelectric devices through parallel connection. *Renew. Energy* **2022**, *193*, 565–575. [CrossRef]
11. Lu, S.; Gu, W.; Meng, K.; Dong, Z.Y. Economic dispatch of integrated energy systems with robust thermal comfort management. *IEEE Trans. Sustain. Energy* **2021**, *12*, 222–233. [CrossRef]
12. Li, Z.M.; Wu, L.; Xu, Y.; Zheng, X.D. Stochastic-weighted robust optimization based bilayer operation of a multi-energy building microgrid considering practical thermal loads and battery degradation. *IEEE Trans. Sustain. Energy* **2021**, *13*, 668–682. [CrossRef]
13. Jiang, B.; Wang, W.; Liu, S.; Wang, Y.; Wang, C.; Chen, Y.; Xie, L.; Huang, M.; He, J. High figure-of-merit and power generation in high-entropy GeTe-based thermoelectrics. *Science* **2022**, *377*, 208–213. [CrossRef] [PubMed]
14. Dado, B.; Gelbstein, Y.; Dariel, M.P. Nucleation of nano-size particles following the spinodal decomposition in the pseudo-ternary $Ge_{0.6}Sn_{0.1}Pb_{0.3}Te$ compound. *Scr. Mater.* **2010**, *62*, 89–92. [CrossRef]
15. Liu, H.T.; Sun, Q.; Zhong, Y.; Deng, Q.; Gan, L.; Lv, F.L.; Shi, X.L.; Chen, Z.G.; Ang, R. High-performance in n-typr PbTe-based thermoelectric materials achieved by synergistically dynamic doping and energy filtering. *Nano Energy* **2022**, *91*, 106706. [CrossRef]
16. Sadia, Y.; Elegrably, M.; Ben-Nun, O.; Marciano, Y.; Gelbstein, Y. Submicron features in higher managanese silicide. *J. Nanomater.* **2013**, *2013*, 701268. [CrossRef]
17. Mahan, G.D. Inhomogeneous thermoelectrics. *J. Appl. Phys.* **1991**, *70*, 4551–4554. [CrossRef]
18. Kuznetsov, V.L.; Kuznetsova, L.A.; Kaliazin, A.E.; Rowe, D.M. High performance functionally graded and segmented Bi2Te3-based materials for thermoelectric power generation. *J. Mater. Sci.* **2002**, *37*, 2893–2897. [CrossRef]
19. Wallace, T.T.; Jin, Z.H.; Su, J. Efficiency of a Sandwiched Thermoelectric Material with a Graded Interlayer and Temperature-Dependent Properties. *J. Electron. Mater.* **2016**, *45*, 2142–2149. [CrossRef]
20. Jin, Z.H.; Wallace, T.T.; Lad, R.J.; Su, J. Energy Conversion Efficiency of an Exponentially Graded Thermoelectric Material. *J. Electron. Mater.* **2013**, *43*, 308–313. [CrossRef]
21. Cao, X.S.; Yang, J.S. Analysis of Thermoelectric Generators with General Material Property Variations. *J. Electron. Mater.* **2019**, *48*, 5516–5522. [CrossRef]
22. Cao, X.; Niu, W.; Cheng, Z.; Shi, J. Power Series Iterative Approximation Solution to the Temperature Field in Thermoelectric Generators Made of a Functionally Graded Temperature-Dependent Material. *J. Electron. Mater.* **2020**, *49*, 5379–5390. [CrossRef]
23. Niu, W.; Cao, X.S.; Hu, Y.F.; Wang, F.F.; Shi, J.P. Theoretical analysis of annular thermoelectric generators made of functionally graded materials. *AIP Adv.* **2021**, *11*, 025333. [CrossRef]
24. Niu, W.; Cao, X.S.; Hu, Y.F.; Wang, F.F.; Shi, J.P. Approximate analytical solution to the temperature field in annular thermoelectric generator made of temperature-dependent material. *IEEE Trans. Electron Devices.* **2021**, *68*, 6386–6392. [CrossRef]
25. Zhang, M.; Wang, J.; Tian, Y.; Zhou, Y.; Zhang, J.; Xie, H.; Wu, Z.; Li, W.; Wang, Y. Performance comparison of annular and flat-plate thermoelectric generators for cylindrical hot source. *Energy Rep.* **2021**, *7*, 413–420. [CrossRef]
26. Cao, Y.; Abu-Hamdeh, N.H.; Moria, H.; Asaadi, S.; Alsulami, R.; Dizaji, H.S. A novel proposed flexible thin-film solar annular thermoelectric generator. *Appl. Therm. Eng.* **2021**, *183*, 116245. [CrossRef]
27. Fatch, H.Y.; Baker, C.A.; Hall, M.J.; Shi, L. High fidelity finite difference model for exploring multi-parameter thermoelectric generator design space. *Appl. Energy* **2014**, *129*, 373–383.
28. Shi, Y.G.; Mei, D.Q.; Yao, Z.H.; Wang, Y.C.; Liu, H.Y.; Chen, Z.C. Nominal power density analysis of thermoelectric pins with non-constant cross sections. *Energy Convers. Manag.* **2015**, *97*, 1–6. [CrossRef]
29. Ali, H.; Sahin, A.Z.; Yilbas, B.S. Thermodynamic analysis of a thermoelectric power generator in relation to geometric configuration device pins. *Energy Convers. Manag.* **2014**, *78*, 634–640. [CrossRef]
30. Fabián-Mijangos, A.; Min, G.; Alvarez-Quintana, J. Enhanced performance thermoelectric module having asymmetrical legs. *Energy Convers. Manag.* **2017**, *148*, 1372–1381. [CrossRef]
31. Niu, P.B.; Shi, Y.L.; Sun, Z.; Nie, Y.H.; Luo, H.G. Thermoelectric ZT enhanced by asymmertric configuration in single-molecule-magnet junctions. *J. Phys. D Appl. Phys.* **2016**, *49*, 45002. [CrossRef]
32. Yilbas, B.S.; Ali, H. Thermoelectric generator performance analysis: Influence of pin tapering on the first and second law efficiencies. *Energy Convers. Manag.* **2015**, *100*, 138–146. [CrossRef]
33. Liu, H.B.; Meng, J.H.; Wang, X.D.; Chen, W.H. A new of solar thermoelectric generator with combination of segmented materials and asymmetrical legs. *Energy Convers. Manag.* **2018**, *175*, 11–20. [CrossRef]
34. Wang, X.J.; Qi, J.; Deng, W.; Li, G.P.; Gao, X.D.; He, L.X.; Zhang, S.X. An optimized design approach concerning thermoelectric generators with frustum-shaped legs based on three-dimensional multiphysics model. *Energy* **2021**, *233*, 120810. [CrossRef]